Assessment of Differential Cross-sections for Hall-thruster Plume Simulation

IEPC-2011-227

Presented at the 32nd International Electric Propulsion Conference, Wiesbaden, Germany September 11–15, 2011

Tyler D. Huismann* and Iain D. Boyd†
University of Michigan, Ann Arbor, MI, 48109, USA

Abstract: Current plume simulation codes typically utilize particle-based models that require various assumptions about inter-particle collision dynamics. A new collision dynamics algorithm is implemented based on experimental measurements of ion-atom interactions for xenon. The new collision dynamics model is used to simulate the plume of a 6 kW Hall thruster. The results of this simulation are compared to previous results that do not utilize the new model, and both simulations are subsequently compared to experimental measurements of plasma properties in the plume. Results based on the new collision dynamics model show an improved agreement with experimental data, relative to previous collision models.

Nomenclature

*Graduate Student Research Assistant, Department of Aerospace Engineering, huismann@umich.edu.
†James E. Knott Professor, Department of Aerospace Engineering, iainboyd@umich.edu.

A	Area
$\vec{B}$	Magnetic field vector
c_e	Mean electron thermal velocity
C_i	Ionization rate
d	Atomic diameter
e	Elementary charge
$\vec{E}$	Electric field vector
$\vec{g}$	Relative velocity vector
$\vec{j}$	Current density vector
m_c	Reduced mass
$\dot{m}$	Mass flow rate
n	Number density
Δt	Simulation timestep
T	Temperature
U, V, W	Mean velocity
$\vec{v}$	Velocity vector
Greek	
ϵ_i	Ionization energy for xenon, 12.7 eV
κ	Thermal conductivity
$\nu_e, \nu_{ei}, \nu_{en}$	Collision frequency
ω	Viscosity temperature exponent
ϕ	Plasma potential
ψ	Electron velocity streamfunction
σ	Plasma conductivity
$\sigma_r, \sigma_{CEX or MEX}$	Collision cross section
θ	Post-collision scattering angle
Subscripts and Superscripts	
$+$, $2+$	Degree of ionization, single-charged and double-charged
d	Discharge
e	Electron, exit
i	Ion
n	Neutral
r	Reference value

I. Introduction

Electric propulsion (EP) devices are rapidly developing, to the point that missions such as SMART-1 and DAWN have utilized EP thrusters as primary propulsion systems .[1,2] Further, due to their higher overall specific impulse (I_{sp}), EP systems play a crucial role in missions with restricted payload requirements. The exhaust plume of a typical EP device plays a significant role in spacecraft integration concerns. For example, the plume of a typical EP device can interact with sensitive spacecraft systems. High-energy ions with large plume divergence angles or back-flowing charge-exchange (CEX) ions can potentially impinge on various spacecraft surfaces, sputtering material away from where it is needed and depositing material where it is unwanted. Additionally, due to their lower thrust densities as compared to traditional chemical-based devices, EP devices frequently must operate for longer durations than chemical systems, increasing the likelihood of accumulated impingement effects. Scientific instrumentation, solar panels, and communications systems can all be impaired due to impingement. Impairment of these systems could lead to subsystem or even complete mission failure; therefore, EP plumes must be thoroughly understood.

EP systems primarily use electric power to produce thrust, as opposed to traditional chemical-based propulsion systems. Characterization of EP device plumes in general, and Hall thruster plumes in particular, is usually achieved by either performing numerical simulation or conducting experiments at ground-based vacuum facilities. One such facility is the Large Vacuum Test Facility (LVTF) at the University of Michigan's Plasmadynamics and Electric Propulsion Laboratory (PEPL). It is the focus of the present study to assess plume simulation accuracy through comparisons of simulation results with experimental measurements conducted previously at PEPL. The present study utilizes a so-called hybrid modeling method, MPIC, to characterize Hall thruster exhaust plumes. This numerical method has been shown to be an effective tool for understanding these plumes.[3–5]

In this paper, a discharge chamber simulation model, HPHall, is applied to a 6 kW, xenon propellant Hall thruster in order to characterize thruster exit conditions. A hybrid-method plume simulation model, MPIC, is then applied in order to investigate the thruster plume in the LVTF. The heavier xenon species are simulated using a direct simulation Monte Carlo (DSMC) method[6] in conjunction with a Particle-in-Cell (PIC) method,[7] such that the effect of particle collisions and internal electric fields are resolved. Additionally, a detailed fluid-electron model is incorporated in place of the standard Boltzmann relation for modeling electrons and is discussed below.[8] The present study focuses on assessing different collision models that are utilized in MPIC. Comparisons between the collision models are made to determine effects on the calculation of plasma parameters. These comparisons are also extended to experimental measurements previously recorded in the plume, in order to determine the effectiveness of the various methods utilized.

II. Facility, Diagnostics, and Thruster Details

The LVTF is a 6 m diameter, 9 m long cylindrical stainless steel vacuum chamber. The facility is shown in Figure 1. The chamber is pumped by seven CVI TM-1200 re-entrant cryo-pumps which are surrounded by liquid nitrogen (LN2) cooled shrouds. The chamber has a total pumping rate of about 240,000 L/s for xenon. This resulted in a back-pressure of approximately 1×10^{-5} torr for nominal operating conditions.

This study will be making comparisons to data acquired using Faraday probes. Characterization of the experimental apparatus is discussed by Reid; further details are included therein.[9] A Faraday probe is a current collecting surface that is large relative to the local Debye length. The probes referenced in this study were voltage-biased in order to repel electrons so that the probes measure only the local ion current density. Faraday probes commonly employ guard-rings around the collecting surface to reduce edge effects that could artificially increase measured data. The experimental data reported in this study were acquired using two different Faraday probe designs: a 23.1 mm diameter tungsten-coated aluminum disk with a guard-ring was used to make far-field plume measurements of current density, while a 4.85 mm diameter molybdenum disk without a guard-ring was used to make near-field plume measurements. The uncertainty in the measurements taken with the far-field probe is due mainly to background gas effects and is conservatively estimated at $+0/-50\%$ on the integrated beam current. The uncertainty in the measurements taken with the near-field probe is due mainly to probe area definition: the near-field probe lacked a guard-ring due to fabrication constraints. The uncertainty is therefore estimated at $\pm 10\%$ on the integrated beam current.

Figure 2 shows the stationary plasma Hall thruster that is the examined in this study. The thruster was operated in the LVTF over a range of operating modes, with the nominal condition being the focus of this

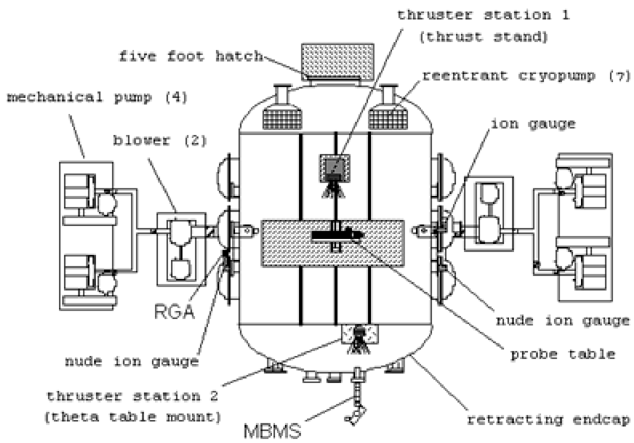

Figure 1. The LVTF. Schematic courtesy of the PEPL.

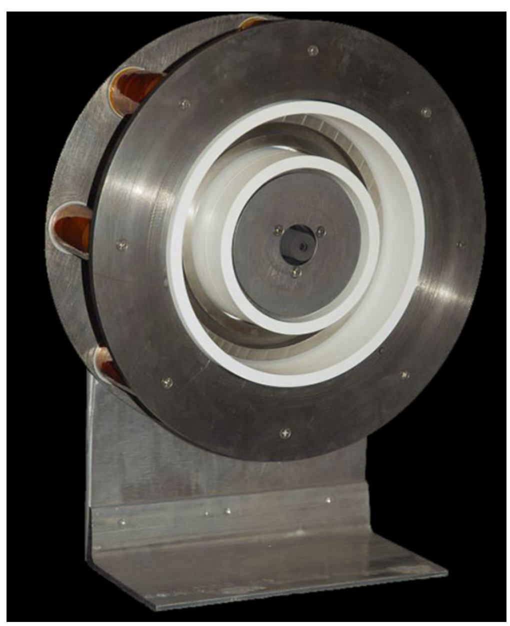

Figure 2. A 6 kW SPT Hall thruster. Photo courtesy of PEPL.

Operating Condition	$\dot{m}_a$	I_d	V_d
Nominal	$20\ \frac{mg}{s}$	$20\ A$	$300\ V$

Table 1. Operating conditions for a 6 kW Hall thruster.

work. The nominal operating conditions are reported in Table 1.

This particular thruster possesses a cathode that is mounted along the thruster centerline, resulting in a completely axisymmetric flow. The thruster's cathode was operated at around 7% of the anode mass flow rate. The thruster is designed to produce 100-600 mN of thrust at 1000-3000 s of I_{sp}, as stated in Ref. 9. For further details of the thruster's operation, see the same reference.

III. Numerical Methods

A. HPHall Methodology

For the past decade, the Hall thruster modeling package HPHall has been the focus of much research and analysis. HPHall models the plasma within the thruster discharge chamber and near-field plume, employing both fluid and particle-in-cell (PIC) numerical methods on an axisymmetric grid.[10] The code has been found to be effective in creating time-averaged outputs of performance data. An example of this time-averaged output of the code can be seen in Figure 3, which is a representation of plasma potential for the thruster operating at the nominal conditions detailed in Table 1.

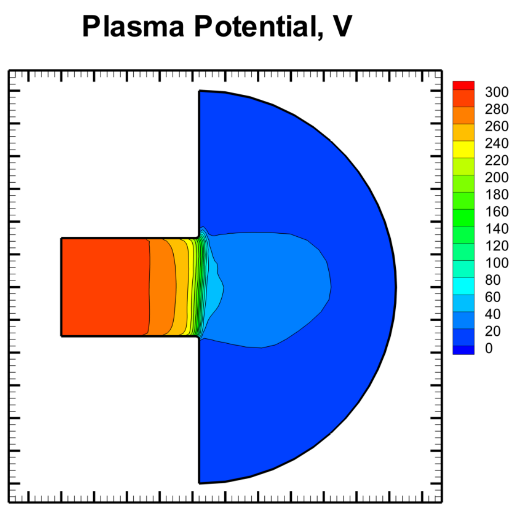

Figure 3. Time-averaged plasma potential contours.

HPHall's development has been documented by Giuliano and Boyd,[11] the main points of which are summarized here. The HPHall code performs an axisymmetric simulation, commonly referred to as "hybrid-PIC," treating the electrons via fluid approximation equations and treating the heavy species, namely xenon ions and atoms, via a particle-in-cell (PIC) method. The electron equations are solved at a smaller time step, called the electron subcycle, in order to accommodate the fact that the speed of electrons is much faster than that of a xenon atom or ion. This allows for electron fluid equations to be fully converged in between xenon particle updates. Hybrid fluid-particle methods have been shown to be successful in Hall thruster plume studies[12] and are computationally more efficient than fully kinetic methods.[13] Through past work, the code has a favorable history of presenting good agreement with macroscopic properties, such as discharge current and thrust, as well as local properties, such as plasma density, plasma potential, and electron temperature.[14–16] For this type of two-dimensional contour plot, the anode is located on the left side and the near-field plume is located on the right side of the domain.

HPHall has been developed to include the capability to output detailed information of each xenon species at various points in the simulation domain. Similar to previous work,[4,5] this capability is utilized in the current study to determine inflow conditions at the thruster exit for plume simulations.

B. MPIC Methodology

1. Heavy Species Submodel

The MPIC simulations use a hybrid model that is constituted by a heavy species submodel and an electron fluid submodel. The heavy species submodel utilizes a DSMC module that handles collisions, and a PIC module that is used to move the heavier particles that are influenced by the electric fields present. Finally, the electrons are simulated using a detailed fluid submodel; this is discussed in Section 2.

The DSMC module handles collisions between the following heavy species: Xe, Xe^+, and Xe^{2+}. The DSMC method uses virtual particles to simulate collisions in rarefied gas flows. The particles represent real ions and neutrals and are grouped in cells whose characteristic lengths are shorter than a mean free path. Pairs of these particles are selected at random and a collision probability is evaluated that is proportional to the product of the relative velocity and collision cross-section. This probability is compared to a random number to determine if the collision occurs. If so, collision dynamics are performed to alter the properties of the colliding particles. Two types of collision dynamics are relevant to Hall thruster plumes: momentum exchange (MEX) collisions and charge exchange (CEX) collisions. MEX collisions involve only exchange of momentum between participating particles. The Hall thruster plume in the present study is confined to two different types of MEX collisions, neutral-neutral collisions and neutral-ion collisions. For neutral-neutral collisions, the variable hard sphere model is employed[6] as follows:

$$\frac{\sigma_{MEX}}{\sigma_r} = \frac{g^{1-2\omega}}{g_r^{1-2\omega}} \tag{1}$$

Here, g_r is the relative collision speed at a reference temperature T_r and σ_r is the reference cross section based on a reference molecular diameter: $\sigma_r = \pi d_r^2$. Assuming $T_r = 273K$, ω and d_r values can be found for several major species in.[6] For neutral-ion MEX collisions, the cross section is based on measurements by Pullins et al.[17] and Miller et al.:[18]

$$\sigma_{MEX}\left(Xe, Xe^+\right) = 1.0 \times 10^{-20}\left(87.3 - 13.6 \log \frac{m_c g^2}{2e}\right) m^2 \tag{2}$$

where m_c is the reduced mass. Based on previous work,[3,19] the present study assumes that MEX and CEX cross sections are similar enough to be equated:

$$\sigma_{MEX}\left(Xe, Xe^+\right) = \sigma_{CEX}\left(Xe, Xe^+\right) \tag{3}$$

$$\sigma_{MEX}\left(Xe, Xe^{2+}\right) = \sigma_{CEX}\left(Xe, Xe^{2+}\right) \tag{4}$$

Pullins et al.[17] and Miller et al.[18] additionally report that the CEX cross section for $Xe - Xe^{2+}$ pairs is approximately half as large as the cross section for $Xe - Xe^+$ pairs at corresponding energies. Therefore, the present study assumes that CEX cross sections are related:

$$\sigma_{CEX}\left(Xe, Xe^{2+}\right) = \frac{1}{2} \times \sigma_{CEX}\left(Xe, Xe^+\right) \tag{5}$$

Once a collision is determined to occur, post-collision properties are calculated. Conservation of momentum and conservation of energy provide four out of the six equations required to calculate post-collision velocities. Typically, assumptions regarding the post-collision velocity direction, or scattering angle, are made to provide the remaining equations. In the present study, the MEX scattering angles are calculated by one of two methods: *i*) isotropic scattering is assumed, or *ii*) statistical scattering based on measured differential cross sections is assumed. Method *i*) treats the angular dependence of the colliding particles as unknown and assigns the direction of the post-collision relative velocity vector at random on a unit sphere. Method *ii*) is based on recent measurements of ion-atom interactions: these data are used to determine the post-collision in-plane relative velocity angles, whereas out-of-plane angles are chosen randomly. Hereafter, MPIC simulations utilizing method i) are named MPIC1-simulations, and those utilizing method ii) are named MPIC2-simulations.

CEX collisions and their effects are modeled by creating an ion moving at the bulk velocity of neutrals at the original ion's location. The original ion is then removed from the list of ions and added to the list of neutrals. Scattering angles for CEX collisions are subsequently calculated one of two ways, corresponding to the two methods for calculating MEX collision scattering angles : i) an analytical distribution is sampled from; ii) a curve fit based on empirical data is sampled from. Since scattering angles for CEX collisions are relatively small due to the lack of momentum transfer, the curve fit in method i) is biased toward low-angles. Figure 4 illustrates the distributions from which methods i) and ii) sample to determine scattering angles for MEX and CEX collisions.

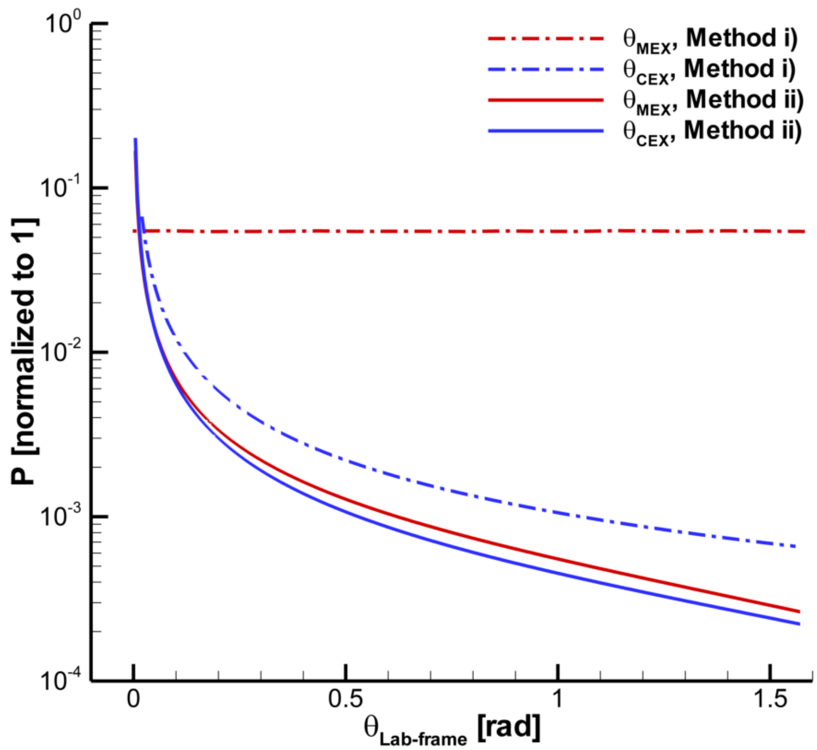

Figure 4. Scattering angle distributions sampled from in DSMC-PIC collisions.

The differences between each heavy species submodel, MPIC1 and MPIC2, are summarized in Table 2. Each label indicates how each post-collision scattering angle is modeled: "$DSMC_{iso}$" indicates the assumption of isotropic scattering; "$DSMC_{ana}$" indicates the assumption of an analytic distribution of scattering angles; "$DSMC_{emp}$" indicates the assumption of a distribution of scattering angles that is fit to empirical data.

In order to represent internal electric fields that characterize plasmas, a PIC module is used to move the heavier ion particles that are influenced by the electric fields. The PIC module determines the charge density at the nodes in the mesh based on the proximity of each particle to the surrounding nodes. The charge density is then used to compute the electric field at each node. This is accomplished either by incorporating the Boltzmann relation or solving for the potential directly using the detailed-fluid model. The potential is then differentiated spatially to obtain the electric fields. Subsequently, acceleration due to the electric field affects the trajectory of heavy species, though accelerations due to magnetic fields are ignored.

Collision Type		MPIC1	MPIC2
MEX	Xe – Xe	$DSMC_{iso}$	$DSMC_{iso}$
	$Xe - Xe^{+}$	$DSMC_{iso}$	$DSMC_{emp}$
	$Xe - Xe^{2+}$	$DSMC_{iso}$	$DSMC_{emp}$
CEX	$Xe - Xe^{+}$	$DSMC_{ana}$	$DSMC_{emp}$
	$Xe - Xe^{2+}$	$DSMC_{ana}$	$DSMC_{emp}$

Table 2. Comparison of collision dynamics methods in heavy species submodels.

2. Electron Fluid Submodel

To reduce computational cost, hybrid-method codes represent electron motion with fluid approximations. For typical thruster conditions, electron collision frequency is almost two orders of magnitude higher than ion collision frequency, and electrons are also several orders of magnitude lighter than ions and move on a much smaller timescale. Therefore, it can be assumed that electrons adjust their velocities much more quickly than ions, making the fluid approximation appropriate. Two types of electron fluid models are typically used: the Boltzmann model, and the detailed fluid model. Although MPIC can utilize either model, the detailed fluid model is used exclusively in the present study.

In order to increase the level of physics as compared to the Boltzmann relation, a detailed fluid electron model was incorporated into the MPIC electron submodel .[3,5,8,19] The detailed fluid model represents the electron fluid using conservation law-type equations: one equation from mass conservation, one equation from momentum conservation, and one equation from energy conservation. Each equation is assumed to describe the electron fluid at steady state and is subsequently transformed such that a fundamental electron property is obtained: electron velocity, plasma potential, and electron temperature, respectively. This transformation also results in a set of Poisson equations with source terms, summarized in Equations (6)- (8):

$$\nabla^2 \psi = n_e n_n C_i \tag{6}$$

$$\begin{aligned} \nabla \cdot (\sigma \nabla \phi) &= \frac{k}{e}\left(\sigma \nabla^2 T_e + \sigma T_e \nabla^2 \ln(n_e) + \sigma \nabla \ln(n_e) \cdot \nabla T_e\right) \\ &+ \frac{k}{e}\left(T_e \nabla \sigma \cdot \nabla \ln(n_e) + \nabla \sigma \cdot \nabla T_e\right) \end{aligned} \tag{7}$$

$$\begin{aligned} \nabla^2 T_e &= -\nabla \ln(\kappa_e) \cdot \nabla T_e + \frac{1}{\kappa_e}\left(-\vec{j} \cdot \vec{E} + \frac{3}{2} n_e (\vec{v_e} \cdot \nabla) k T_e\right) \\ &+ \frac{1}{\kappa_e}\left(3 \frac{m_e}{m_i} \nu_e n_e k (T_e - T_h) + n_e n_n C_i \epsilon_i\right) \end{aligned} \tag{8}$$

This system is treated in the current study in the same manner as in Refs. 3 and 22, the results of which are summarized as follows. By treating the right-hand side as known in Eqs. (6)- (8), three fundamental plasma parameters are solved for, namely $\vec{v}_e$, ϕ, and T_e. This is achieved by expressing the system as a generalized Poisson equation and solving the system with a finite element solver. Derivative calculation is handled by a least squares method, also presented in Refs. 3 and 22.

C. Boundary Conditions

For computations of a Hall thruster plume in the LVTF, boundary conditions must be specified at the thruster exit, outflow surfaces, chamber centerline, and along the thruster wall, for both the heavy species submodel and the electron fluid model. Figure 5 shows a schematic of the grid utilized in the current study. First, the boundary conditions for the heavy species submodel are presented, followed by those for the electron fluid submodel.

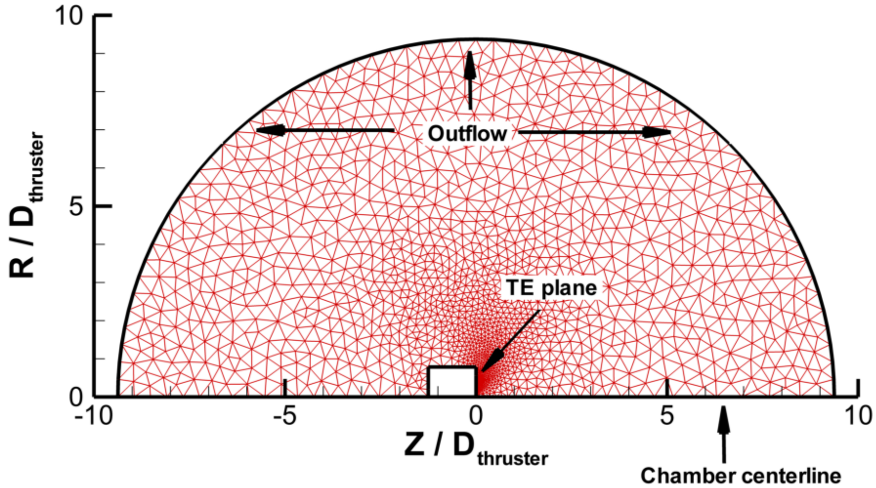

Figure 5. Schematic of axisymmetric, unstructured grid, normalized by mean thruster diameter.

Some of the macroscopic properties of the plasma are required at the thruster exit (TE), namely the number density, velocity components, and temperature of each heavy species in the calculation. The TE plane is discretized into three line segments of equal length, S_1, S_2, and S_3, with the middle segment, S_2, centered on the acceleration chamber centerline. Since HPHall is a particle method, the inflow properties for the plume simulations are extracted from HPHall and are tabulated below. To determine particle properties at the cathode, the assumption is made that the mass flow consists solely of neutral xenon atoms. This assumption allows for a clear calculation of boundary conditions for the fluid electron model, as injecting xenon ions from the cathode creates a current density which feeds back into determination of the fluid boundary conditions. The neutrals are assumed to have a characteristic temperature of 1300 K.[20] The neutrals injected at the cathode are assumed to have sonic velocity, which, using the reported mass flow rate of 7% of the anode mass flow rate[9] and the cathode orifice area, thereby determines the number density. The particle properties for species at the cathode are appended to the tabulated TE data in Table 3.

There is only one solid surface that is modeled in the present analysis, namely the thruster itself. It is assumed to have a plasma potential of zero, i.e. to be electrically grounded. All ions that collide with the thruster wall are neutralized. For the particles scattered back into the flow field from the thruster wall, diffuse reflection is assumed which is characterized by the surface temperature of 300 K.

The facility back-pressure is modeled through static background particles. Each cell contains a few particles with velocities sampled from a zero-centered Maxwellian velocity distribution function at an assumed temperature of 295 K. These particles participate in collisions with plume particles and change the velocities of other particles, but their positions and velocities do not change. The back-pressure value for these simulations is set to the value of the general operation back pressure, 1.0×10^{-5} torr.

The boundary conditions for the detailed-fluid model must be determined in order to solve the conservation equations shown in Section 2. Since each equation is Laplace-like, each one requires specification of either a Dirichlet (direct) value, or a von Neumann (gradient) value. Thus the plasma potential, the electron temperature, and the quantity $\nabla\psi$, i.e. $n_e v_{e,\hat{n}}$, are specified as either direct or gradient values at each boundary in the simulation. Each boundary condition is direct except for the following: *i*) each boundary

Species	Location	U, m/s	V, m/s	T, K	n, m^{-3}
Xe	S_1	420	190	900	7.80×10^{17}
	S_2	710	-40	2800	1.65×10^{17}
	S_3	425	-170	930	7.74×10^{17}
	$Cathode$	320	0	1300	1.78×10^{20}
Xe^+	S_1	11000	100	14600	4.08×10^{17}
	S_2	13100	-360	4000	4.05×10^{17}
	S_3	12900	-500	12900	3.71×10^{17}
	$Cathode$	0	0	0	0
Xe^{2+}	S_1	16500	-870	30100	3.78×10^{16}
	S_2	17400	-400	11000	6.55×10^{16}
	S_3	17500	-220	29900	4.00×10^{16}
	$Cathode$	0	0	0	0

Table 3. Heavy species inflow conditions at the TE plane and cathode. TE plane conditions extracted from HPHall. Note: all out of plane velocities are set to zero.

Species	Location	ϕ, V	$\nabla\psi$, $m^{-2}\ s^{-1}$	T_e, eV
e^-	S_1	166	-5.243×10^{21}	32.5
	S_2	179	-7.010×10^{21}	31.1
	S_3	138	-6.475×10^{21}	29.8
	$Cathode$	4	3.251×10^{24}	3.0
	$Wall$	0	0	0
	$Symmetry$	0	0	0
	$Outflow$	0	0	3.0

Table 4. Electron submodel boundary conditions. TE plane conditions extracted from HPHall.

condition for the axis of symmetry is a gradient-type condition, *ii*) the wall of the thruster has a gradient-type condition for the electron temperature, and *iii*) the outflow surface has a gradient-type condition for $n_e v_{e,\hat{n}}$ and ϕ. The value to which each is set is specified in Table 4.

Due to the grounding of the thruster, the plasma potential condition is direct and set to zero for the thruster walls. At the TE plane and the cathode, the plasma potential is set to values from HPHall. The electron temperature is also set to characteristic values based on HPHall. The TE plane boundary condition for $n_e v_{e,\hat{n}}$ is determined using electron current density information from HPHall:

$$n_e v_{e,\hat{n}} = \frac{\vec{j}_e}{e} \tag{9}$$

The cathode boundary condition for $n_e v_{e,\hat{n}}$ is determined by the discharge current and cathode area as follows:

$$n_e\, v_{e,\hat{n}} = \frac{I_d}{e\, A_{cathode}} \tag{10}$$

In summary, the electron submodel boundary conditions utilized in this study are shown in Figure 6.

IV. Results

The plume simulations presented in the present work use either the MPIC1 or MPIC2 heavy species submodel as outlined in Section 1 and the detailed fluid electron submodel as outlined in Section 2. Plume

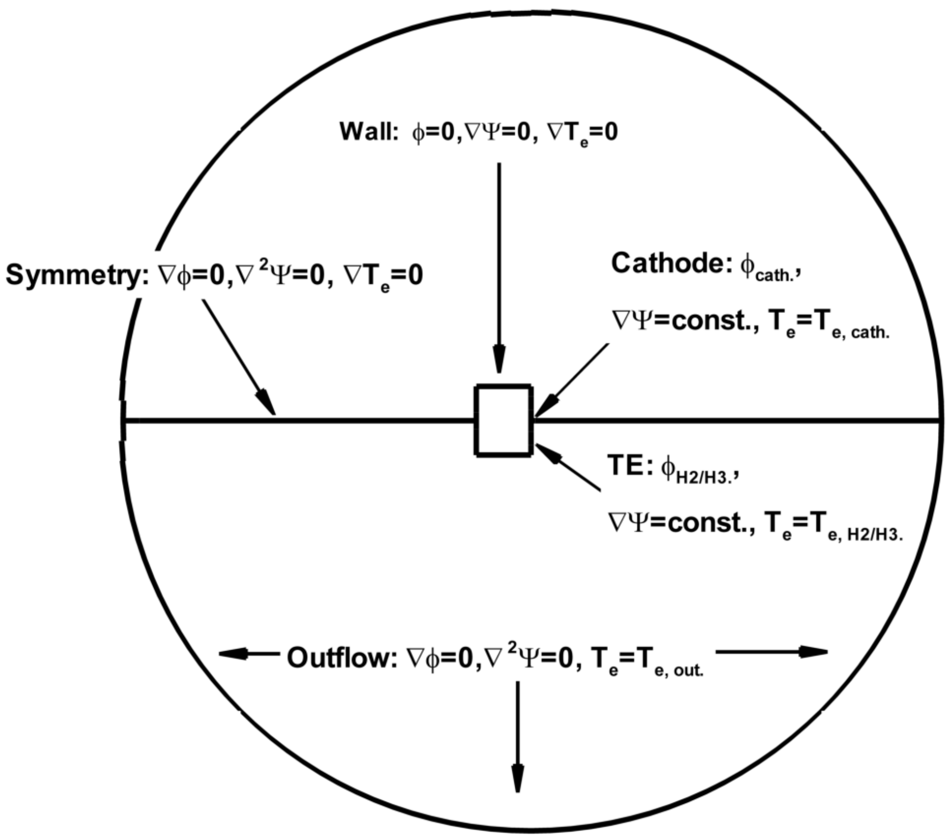

Figure 6. Boundary conditions for the electron submodel.

simulations utilizing the MPIC1 heavy species submodel are dubbed "MPIC1-simulation(s)," and those utilizing the MPIC2 submodel are dubbed "MPIC2-simulation(s)." The plume simulation runs for 350,000 timesteps to reach a steady state and then for another 100,000 timesteps to sample macroscopic data. This results in a total of approximately 2.5 million particles at steady state over the domain shown in Figure 5, where the domain consists of 3,191 triangular cells with 50-6000 macroparticles per cell. The timestep size is 1×10^{-7} seconds, resulting in a total sampling time of 0.01 seconds. All simulations are run in parallel on the University of Michigan Center for Advanced Computing's Nyx cluster. All simulations utilized 32 processors, with a computational wall time around 12 hours for MPIC1-simulations and around 15 hours for MPIC2-simulations.

Note that all results use spatial coordinates that are normalized by a characteristic length associated with the thruster, in this case, the mean thruster diameter. The primary difference between MPIC1- and MPIC2-simulation is in the heavy species submodel that each utilize, therefore comparisons between the plume simulations are made through examining heavy species properties, namely: particle velocity, number density, and ion current density. Comparisons between the simulations and experimental data are made through examining ion current density. The comparisons focus primarily on the near-field plume region, between 0-3 mean thruster diameters downstream of the TE plane, and between 0-2.5 mean thruster diameters radially from the thruster centerline. There is an additional comparison made using far-field plume data taken in a 180° circular arc with a radius of approximately 1 m and an origin on the axis in the TE plane. All comparisons are represented by extraction lines in Figure 7.

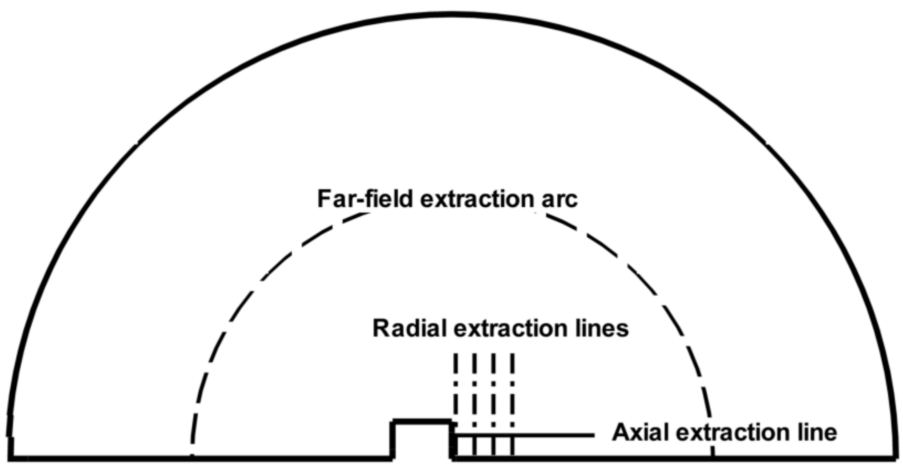

Figure 7. Extraction lines utilized in plume comparisons.

A. Evaluating Post-collision Scattering Models

1. Ion Velocity

In this section, velocity data for the ionized heavy species particles are presented for MPIC1- and MPIC2-simulation. Field contours of axial velocity of Xe^{+} and Xe^{2+} are shown in Figures 8 and 9, whereas contours of radial velocity are shown in Figures 10 and 11. Subsequent figures present data that are extracted from this field data. The primary difference between MPIC1-simulations and MPIC2-simulations is in the magnitude of the peak axial and peak radial velocity of both species. The peak axial velocity of Xe^+ calculated by MPIC2-simulation is 8% higher than that calculated by MPIC1-simulation, relative to MPIC1, whereas the peak axial velocity of Xe^{2+} calculated by MPIC2-simulation is 6.5% higher than that calculated by MPIC1-simulation, relative to MPIC1. The peak radial velocity of Xe^+ calculated by MPIC2-simulation is 9% higher than that calculated by MPIC1-simulation, relative to MPIC1, whereas the peak radial velocity of Xe^{2+} calculated by MPIC2-simulation is 4% higher than that calculated by MPIC1-simulation, relative to MPIC1.

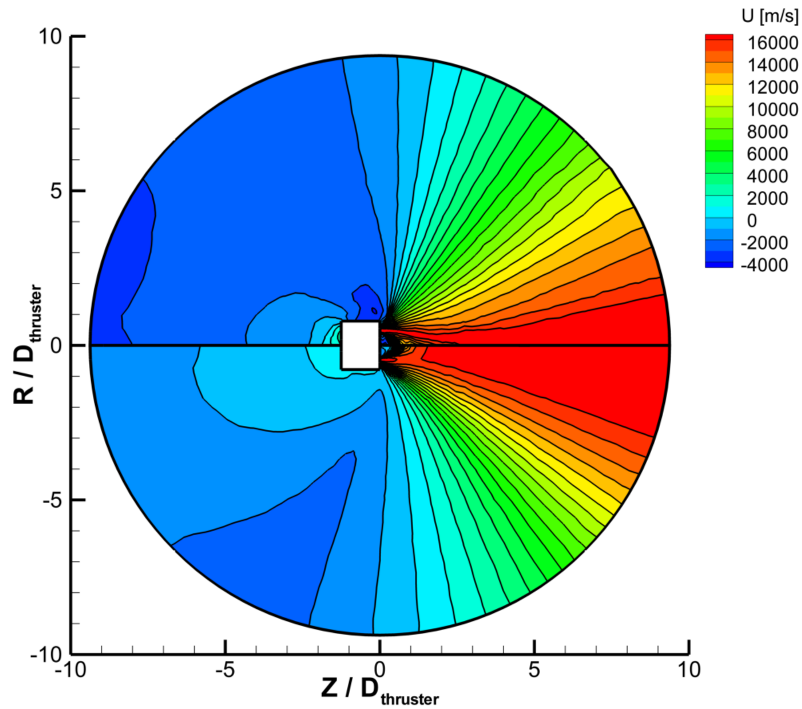

Figure 8. Comparison between MPIC1-simulation (bottom) and MPIC2-simulation (top): axial velocity contours of Xe^+.

The increase in the peak magnitude of velocity of Xe^+ and Xe^{2+} ions is a direct effect of the difference in collision dynamics model between MPIC1 and MPIC2. In MEX collisions between atoms and ions, the post-collision scattering angle distribution that is sampled from in MPIC2-simulation is more heavily weighted toward low-angle scattering than the distribution used in MPIC1-simulation. This results in fewer high-angle scattering MEX collisions in MPIC2 relative to MPIC1, such that axial velocity of ions is not altered by MEX collisions in MPIC2 to the same degree it is affected in MPIC1: plume divergence is decreased in MPIC2 relative to MPIC1. Thus, the main ion beam is more collimated as calculated by MPIC2-simulation than MPIC1-simulation.

Further, the magnitude of peak radial velocity is higher in MPIC2-simulation than MPIC1-simulation. The peak magnitude radial velocity is due primarily to CEX collisions in the near-field plume. MPIC2-simulation calculates post-scattering angles for CEX interactions utilizing a distribution that is more heavily weighted to low-angle scattering than the distribution used in MPIC1-simulation. Although the individual particles are scattered at low-angles in the center of mass (COM) frame, CEX collisions additionally swap particle charges. Thus, fast moving ions with low plume divergence angle as measured in the lab frame collide with slow moving background neutrals and scatter as fast moving neutrals moving at a low plume divergence angle; however, the background neutrals scatter as slow moving ions moving at a high plume divergence angle, as measured in the lab frame. This process is illustrated in Figure 12. Therefore, the peak radial velocity of Xe^+ and Xe^{2+} is increased in MPIC2-simulation relative to MPIC1-simulation, for the same reasons given above regarding the peak axial velocity.

Figures 13 and 14 illustrate angular distributions of axial and radial velocity along a 1 m arc for Xe^+ and Xe^{2+}, respectively. Figures 13 and 14 show the same behavior described above: the peak magnitude of

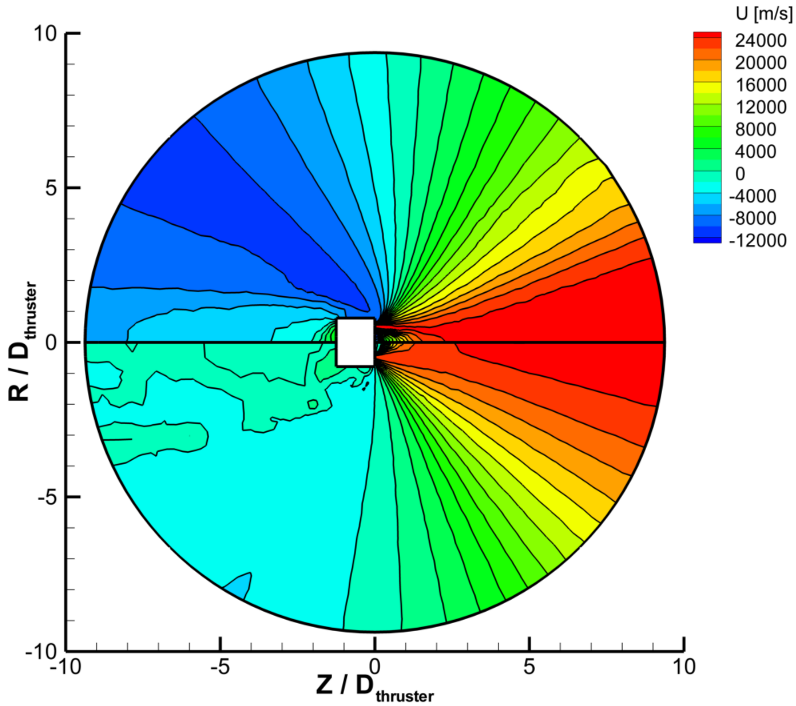

Figure 9. Comparison between MPIC1-simulation (bottom) and MPIC2-simulation (top): axial velocity contours of Xe^{2+}.

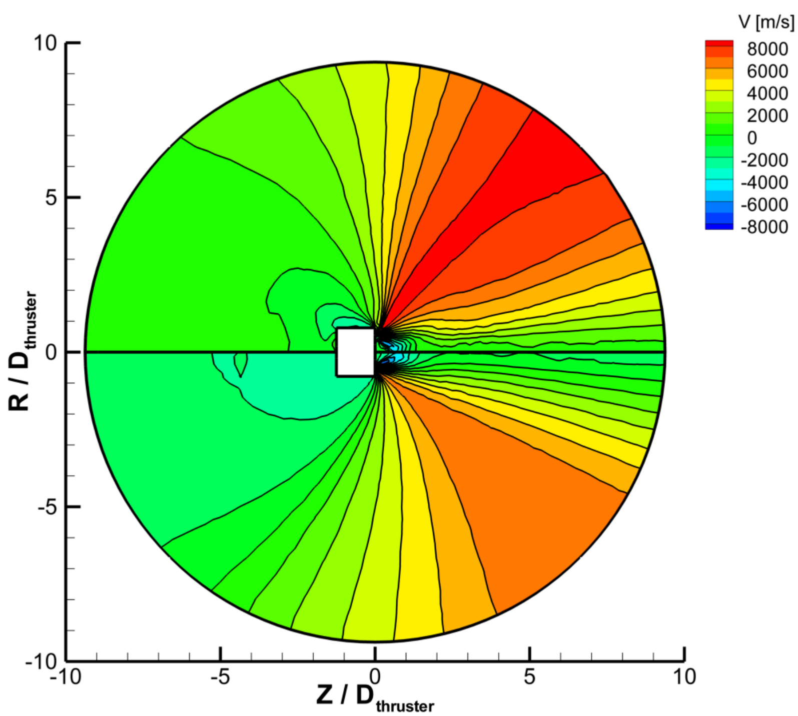

Figure 10. Comparison between MPIC1-simulation (bottom) and MPIC2-simulation (top): radial velocity contours of Xe^{+}.

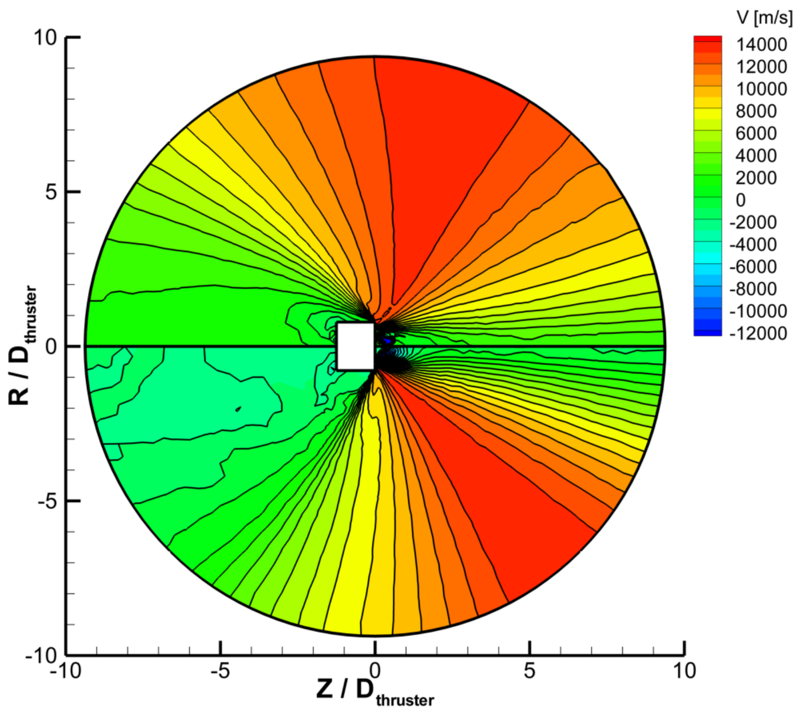

Figure 11. Comparison between MPIC1-simulation (bottom) and MPIC2-simulation (top): radial velocity contours of Xe^{2+}.

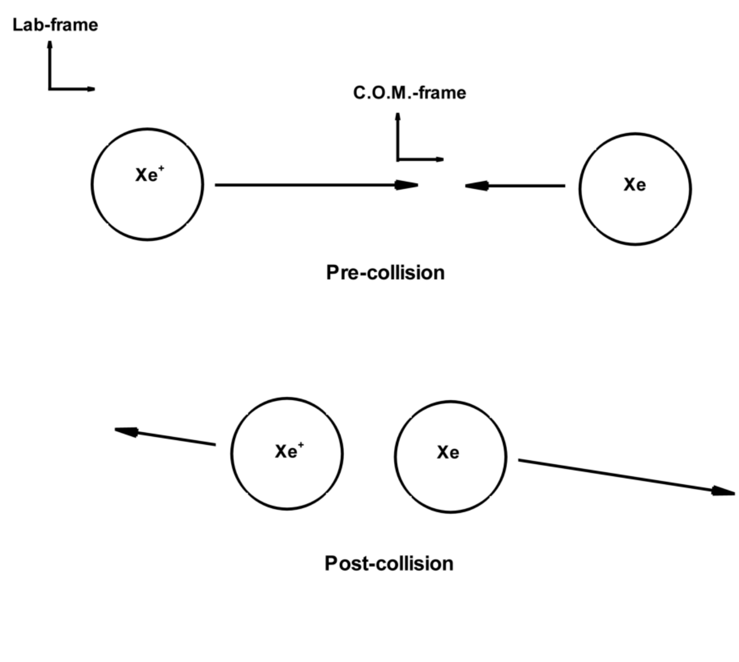

Figure 12. CEX collision schematic.

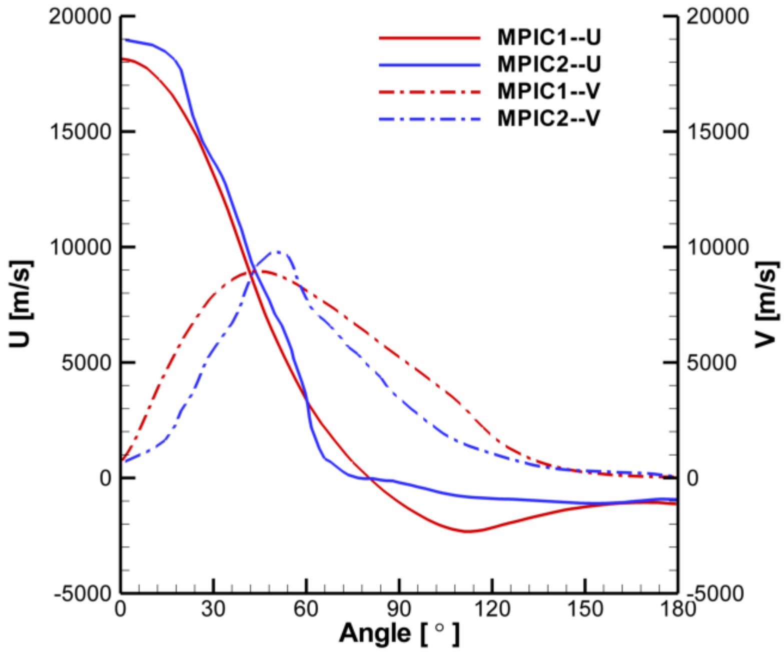

Figure 13. Comparison between MPIC1-simulation and MPIC2-simulation: axial and radial velocity distribution for Xe^{+}along a 1 m arc.

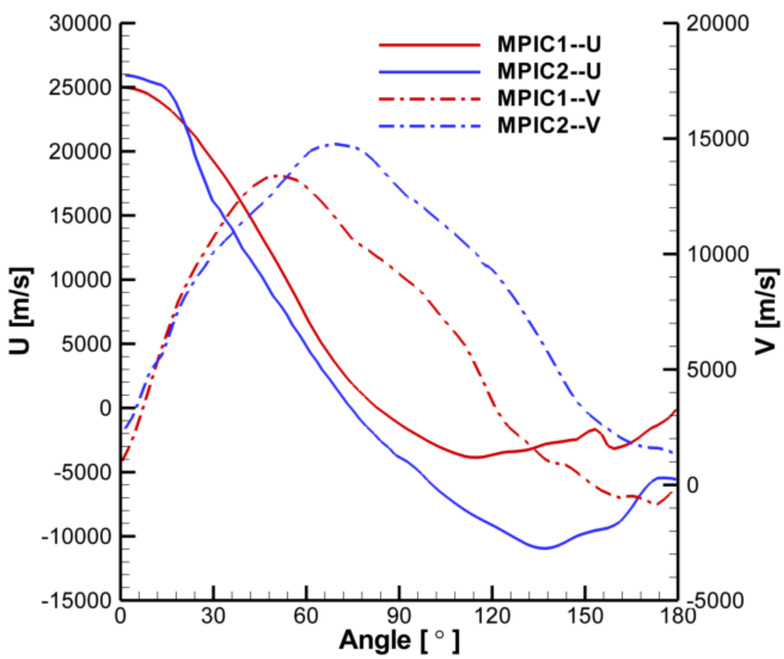

Figure 14. Comparison between MPIC1-simulation and MPIC2-simulation: angular axial and radial velocity profiles for Xe^{2+} along a 1 m arc .

axial and radial velocity is increased in MPIC2-simulation relative to MPIC1-simulation.

2. Ion Number Density

In this section, number density data for the ionized heavy species particles are presented for MPIC1- and MPIC2-simulation. Field contours of Xe^{+} and Xe^{2+} number density are shown in Figures 15 and 16. Subsequent figures present data that are extracted from this field data. The primary difference between MPIC1-simulations and MPIC2-simulations is in the qualitative shape of the data. MPIC2-simulation calculates a number density field with a greater number of ions at higher plume divergence angles than MPIC1-simulation: the familiar CEX "wings" in MPIC2-simulation extend farther upstream of the TE plane than in MPIC1-simulation. This difference is due primarily to the difference in post-collision scattering angle distribution between MPIC1 and MPIC2, as explained in Section 1: MPIC2 utilizes a distribution that is weighted toward low-angle scattering more heavily than the MPIC1 distribution. The increased number density at high plume divergence angles is the effect of this difference in distribution, as shown in Figure 17.

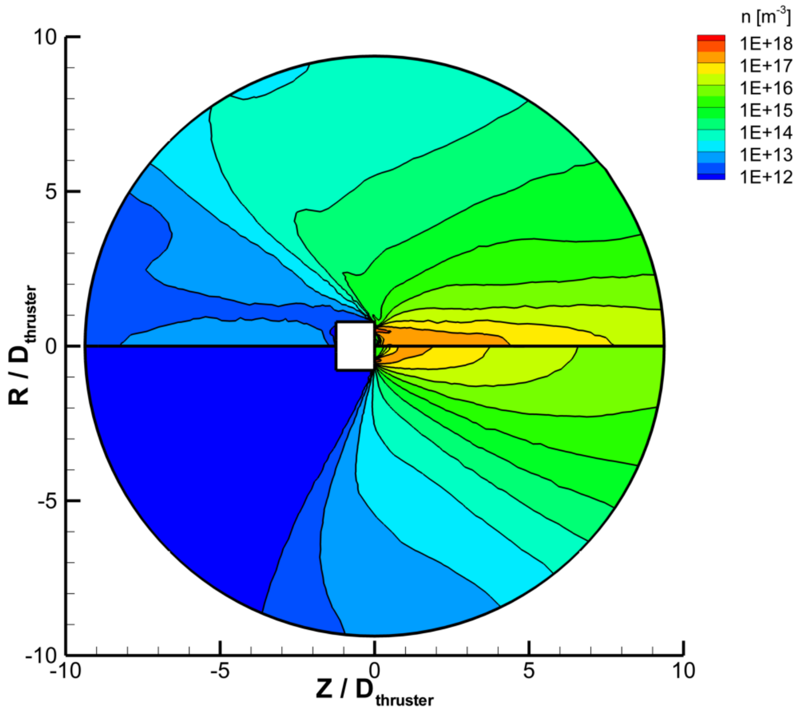

Figure 15. Comparison between MPIC1-simulation (bottom) and MPIC2-simulation (top): number density contours of Xe^{+}.

3. Ion Current Density

In this section, ion current density data are presented for MPIC1- and MPIC2-simulation. Field contours of ion current density are shown in Figure 18. Subsequent far-field data are extracted from this field data. Note that axial and radial profiles of near-field ion current density calculated in MPIC2-simulation are very similar to those profiles calculated by MPIC1-simulation; as such, these profiles are shown in Section IV.B, alongside experimental data.

The main difference between MPIC1-simulations and MPIC2-simulations is exhibited in the far-field plume structure: at high plume divergence angles, MPIC2-simulation calculates an increased magnitude of ion current density relative to MPIC1-simulation. Additionally, MPIC2-simulation calculates a more collimated main beam of ions than MPIC1-simulation: MPIC2-simulation calculates a main ion beam which persists downstream farther than the beam calculated by MPIC1-simulation.

These two differences in plume structure correspond to the differences shown in Sections 1 and 2. The MPIC2 collision dynamics model effectively redistributes plume ions, focusing them more toward both lower

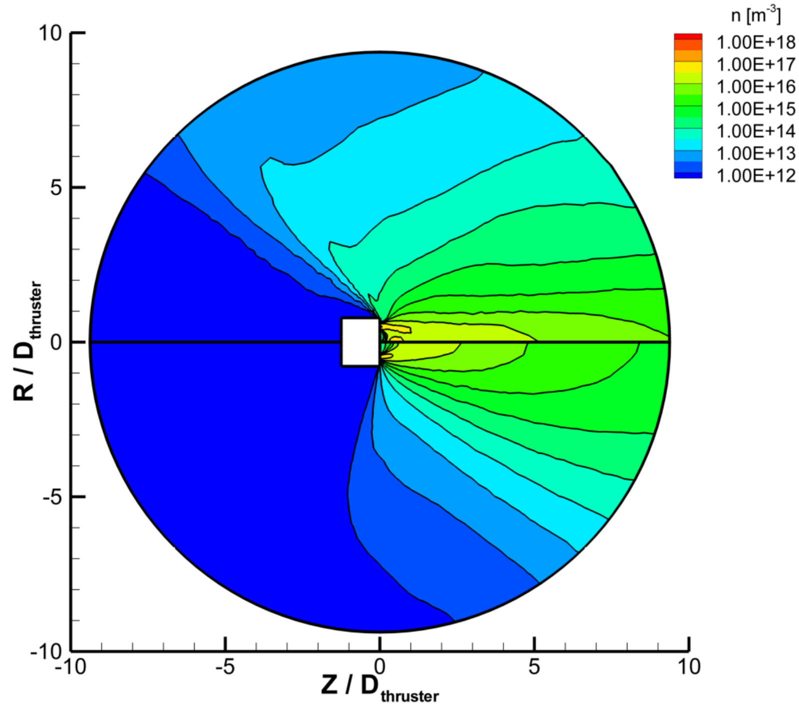

Figure 16. Comparison between MPIC1-simulation (bottom) and MPIC2-simulation (top): number density contours of Xe^{2+}.

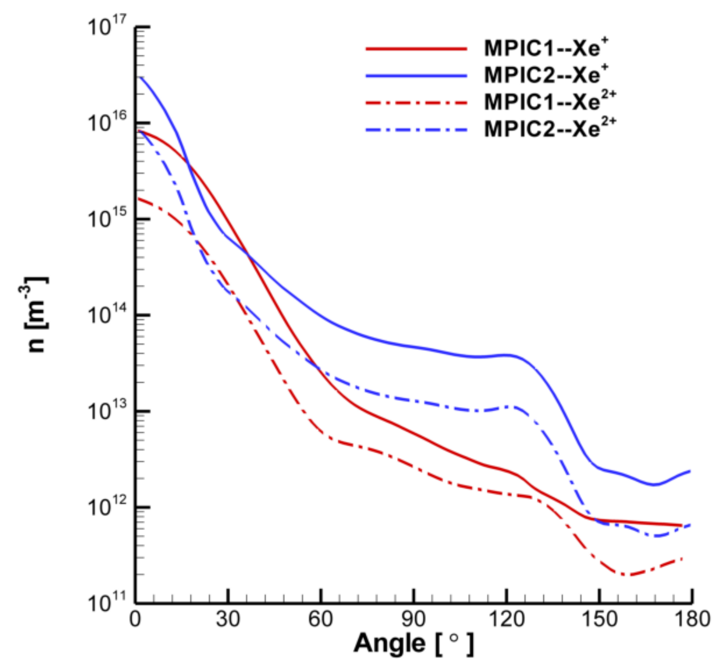

Figure 17. Comparison between MPIC1-simulation and MPIC2-simulation: angular ion number density profiles along a 1 m arc.

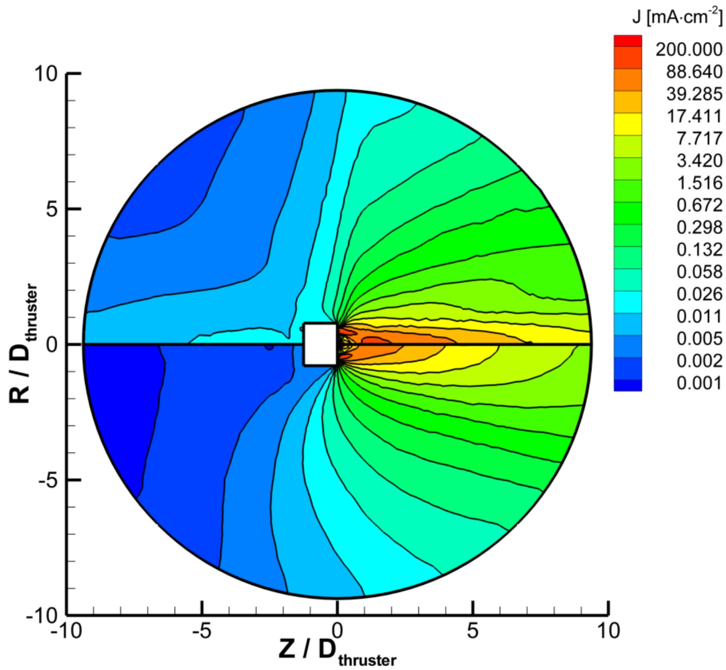

Figure 18. Comparison between MPIC1-simulation (bottom) and MPIC2-simulation (top): ion current density contours.

and higher plume divergence angles and away from mid-range plume divergence angles, relative to MPIC1. Figure 19 illustrates this behavior: at angles less than 5°, MPIC2-simulation calculates an ion current density greater than that calculated by MPIC1-simulation; between 5°-80°, MPIC1-simulation calculates an ion current density greater than that calculated by MPIC2-simulation; and between 80°-150°, MPIC2-simulation again calculates an ion current density greater than MPIC1-simulation.

B. Comparing simulations and experimental data

Experimental measurements of ion current density were performed by Reid.[9] Ion current density measurements are acquired using the near- and far-field Faraday probe, as outlined in Section II. The uncertainty associated with the near-field probe measurements is ±10%, whereas the uncertainty associated with the far-field probe measurements is $\pm 0 - 50\%$ on the integrated beam current. The near-field data is presented first, followed by the far-field data.

1. Near-field Ion Current Density

The near-field ion current density contours reported here are formed from over 64,000 individual measurements.[9] Subsequent comparisons of ion current density profiles are extracted from this experimental data set. It should be noted here that these measured data were not corrected for sheath growth, edge effects, or cosine losses.

Figure 20 shows comparison of the measurements to near-field ion current density calculations in MPIC1-simulation, whereas Figure 21 shows comparison of the measurements to calculations in MPIC2-simulation. MPIC2-simulation calculates near-field plume structure similar to that calculated by MPIC1-simulation: both simulations, as well as the experimental data, show the beam of ions at the TE plane to be highly collimated over the first mean thruster diameter. Both MPIC1- and MPIC2-simulation generally overpredict the magnitude of ion current density relative to the measured data, with MPIC2-simulation overpredicting by a larger factor than MPIC1-simulation. The measured peak ion current density for the main beam is 128 $\frac{mA}{cm^2}$ and occurs at $Z/D_{\text{thruster}} = 0.2$ and $R/D_{\text{thruster}} = 0.5$, whereas the simulations calculate ion current densities of approximately 145 $\frac{mA}{cm^2}$ and 162 $\frac{mA}{cm^2}$ at the same location for MPIC1- and MPIC2-simulation

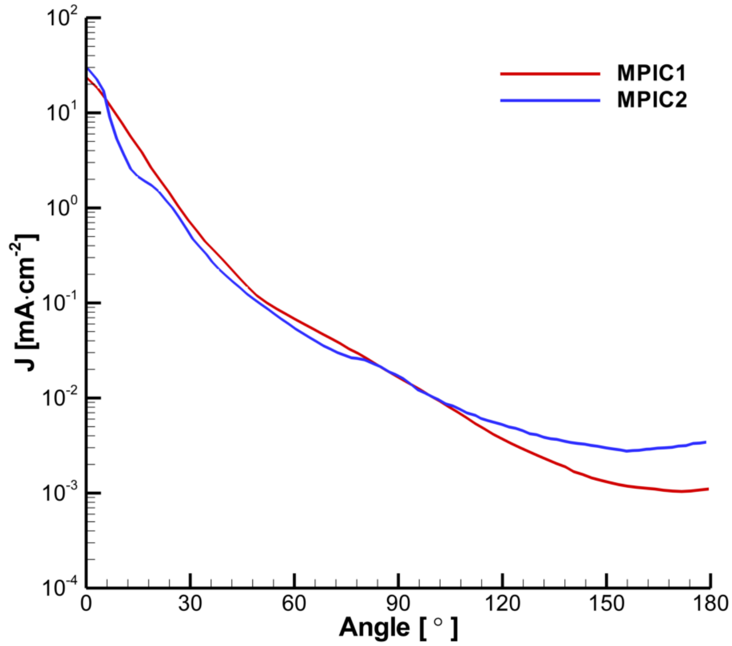

Figure 19. Comparison between MPIC1-simulation and MPIC2-simulation: angular ion current density profiles along a 1 m arc.

respectively. Due to its collision model, MPIC2-simulation calculates a more highly collimated main ion beam than MPIC1-simulation, with the result that, in the near-field plume, agreement between MPIC2-simulation and measured data is not as good as agreement between MPIC1-simulation and measured data. However, both MPIC1- and MPIC2-simulation calculate a higher peak ion current density than the measured peak, even when accounting for measurement uncertainty of +10%. The discrepancy could be due to the placement of the investigation window for the measurements: the calculated peak ion current densities for the main beam occur at $Z/D_{\text{thruster}} = 0.05$, which is nearly coincident with the edge of the window. More likely, however, this might be due to the electron submodel utilized in MPIC: neglecting the $\vec{B}$ field has the largest impact near the TE plane, where gradients in plasma potential are under-predicted, relative to measured data. This results in an under-prediction of electric field magnitude and subsequent under-acceleration of ions, which in turn increases ion current density, relative to measured data.

The axial profiles in Figure 22 show qualitative agreement between the measured data and the calculated ion current densities: for $Z/D_{\text{thruster}} > 0.3$, ion current density monotonically decreases. In general, MPIC1- and MPIC2-simulation show similar agreement with the measured data, although MPIC2-simulation overpredicts ion current density at $Z/D_{\text{thruster}} > 1.5$ to a greater degree than MPIC1, relative to the measured data. Typically, at $Z/D_{\text{thruster}} > 1.5$, the measurements show a higher rate of decay relative to either simulation. Additionally, between $Z/D_{\text{thruster}} = 0.05 - 0.2$, measured data actually shows an increase in ion current density, whereas both simulations calculate a decrease in ion current density due to the same limitations of the electron submodel discussed above.

Figures 23- 26 show radial profiles of ion current density as calculated by MPIC1- and MPIC2-simulation compared to measured data. Figure 23 shows radial profiles at an axial station of $Z/D_{\text{thruster}} = 0.08$. Agreement between the simulations and the measured data is similar: both MPIC1- and MPIC2-simulation underpredict the centerline "spike" in ion current density in the near field plume, relative to the measured data. The "spike" as discussed previously[9] is due to both non-zero radial velocity of ions at the TE plane, as well as the plasma potential field focusing ions toward the thruster centerline. When compared to measured data, MPIC1-simulation underpredicts the magnitude of the centerline spike by approximately 31%, whereas MPIC2-simulation underpredicts the magnitude by approximately 28%, an improvement of 9.6%. There are two possible explanations for the remaining discrepancy. First, the plasma potential field calculated by

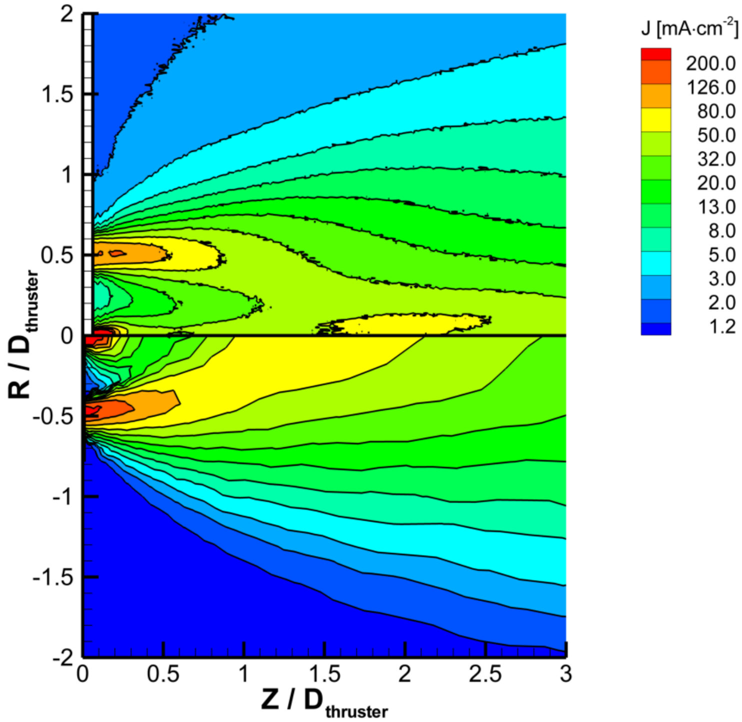

Figure 20. Comparison of ion current density between experimental measurements (top) and MPIC1-simulation (bottom).

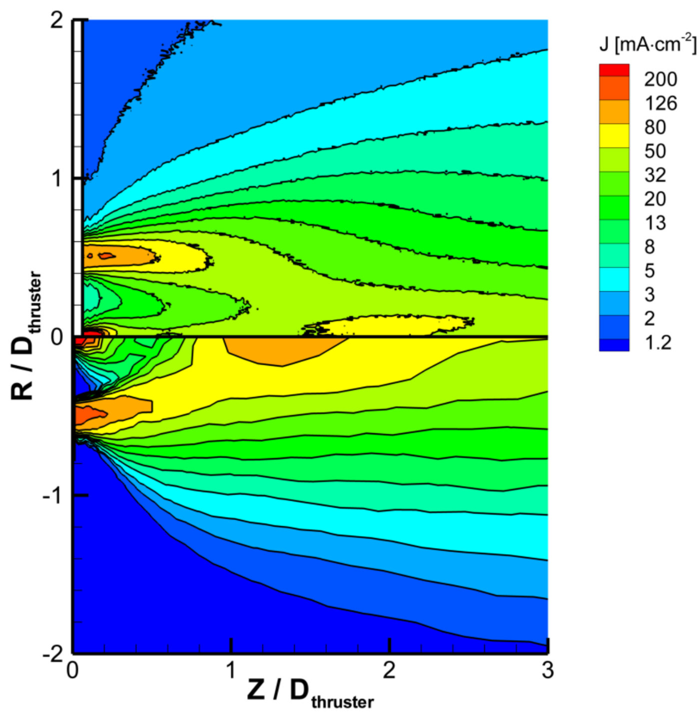

Figure 21. Comparison of ion current density between experimental measurements (top) and MPIC2-simulation (bottom).

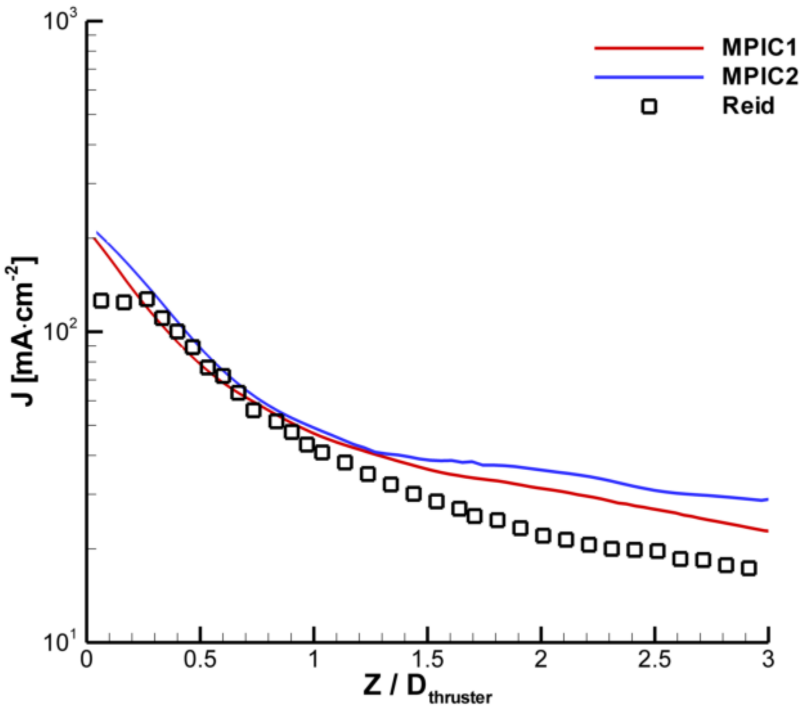

Figure 22. Comparison between MPIC1-simulation, MPIC2-simulation, and experimental measurements: axial ion current density variation along $R/D_{thruster} = 0.5$.

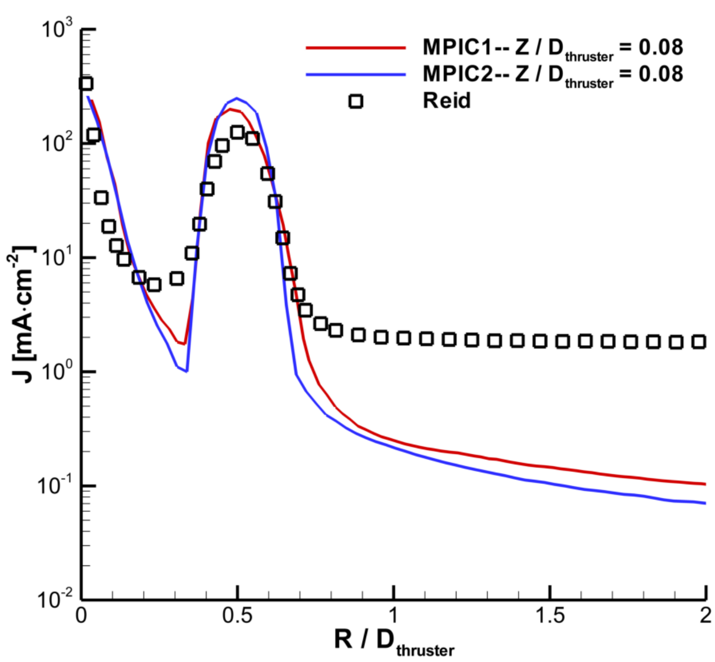

Figure 23. Comparison between MPIC1-simulation, MPIC2-simulation, and experimental measurements: radial ion current density variation along $Z/D_{thruster} = 0.08$.

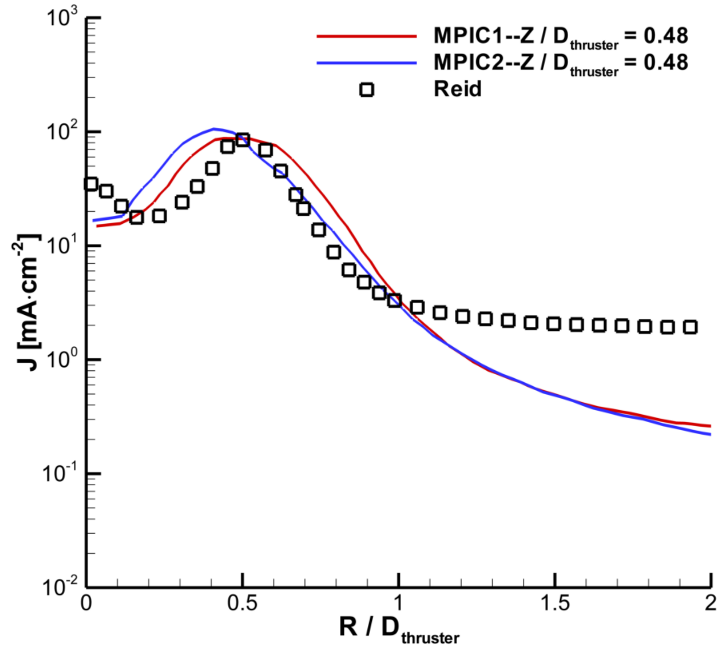

Figure 24. Comparison between MPIC1-simulation, MPIC2-simulation, and experimental measurements: radial ion current density variation along $\mathrm{Z/D_{thruster}} = 0.48$**.**

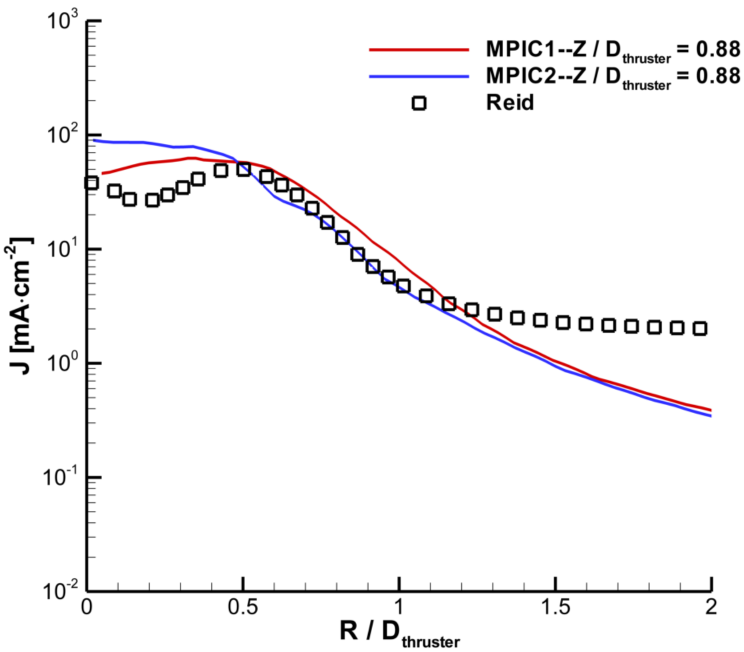

Figure 25. Comparison between MPIC1-simulation, MPIC2-simulation, and experimental measurements: radial ion current density variation along $\mathrm{Z/D_{thruster}} = 0.88$**.**

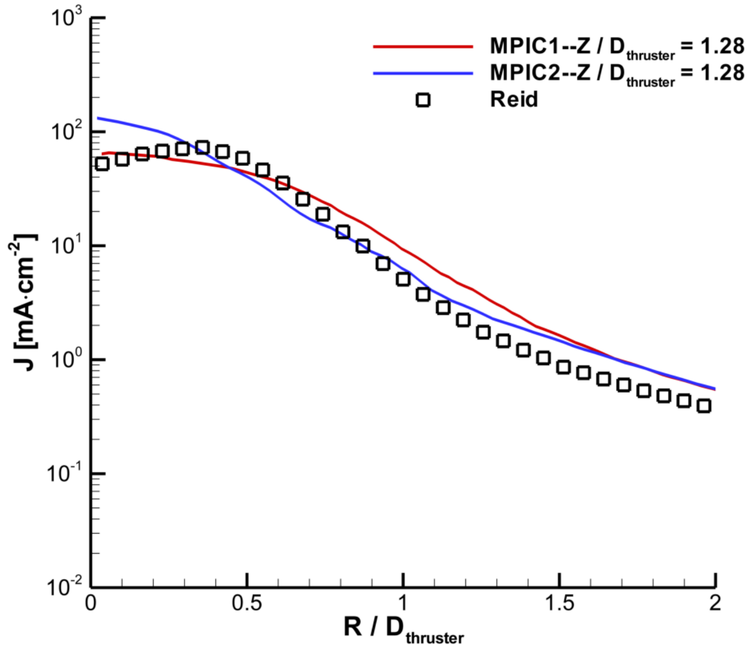

Figure 26. Comparison between MPIC1-simulation, MPIC2-simulation, and experimental measurements: radial ion current density variation along $Z/D_{thruster} = 1.28$**.**

MPIC1- and MPIC2-simulation ignores $\vec{B}$ field effects, which are important in the near-field plume. Second, the current boundary condition assumed at the cathode injects solely neutral atoms into the simulation domain. This assumption is made for the sake of theoretical clarity, but may not accurately reflect the physical situation.

Figures 24- 26 show the behavior of radial profiles of ion current density as $Z/D_{thruster}$ increases. There is a discrepancy in the profile behavior at $R/D_{thruster} > 0.8$: both MPIC1- and MPIC2-simulation calculate steady decay of ion current density in this region, whereas the measured ion current density remains nearly constant at around 1.9 $\frac{mA}{cm^2}$. As noted above, the ion current density measurements in the near-field were made with a Faraday probe that did not have a guard ring. As a result, the probe is susceptible to collecting a non-trivial amount of CEX ions at far off-axis locations .[21] Since the measured data were not corrected for edge effects, the plateau in measured ion current density at far off-axis locations is not solely a measure of the beam current.

Accordingly, Figures 24- 26 show moderate qualitative agreement between simulation and measurements, although significant plume structures are resolved differently when comparing simulated results to the measured data. Due to the underprediction of the centerline spike in ion current density, MPIC1- and MPIC2-simulation calculate a coalescence of the centerline beam into the main ion beam at just over $Z/D_{thruster} = 0.48$, whereas measurements indicate two distinct beams as far downstream as $Z/D_{thruster} = 0.88$. Other qualitative features show better agreement between simulation and measurements: the measured magnitude of the main beam ion current density shows good agreement with simulation, where MPIC2-simulation does show better qualitative agreement with measured data than MPIC1-simulation as $Z/D_{thruster}$ increases. Again, at far off-axis locations, the ion current density measurements at $Z/D_{thruster} = 0.48$ and $Z/D_{thruster} = 0.88$ exhibit a plateau at around 1.9 $\frac{mA}{cm^2}$.

2. Far-field Ion Current Density

Figure 27 shows comparisons of angularly resolved far-field ion current density. The measured data shown here were acquired with the far-field Faraday probe outlined in Section II. Qualitative agreement between MPIC1-simulation is good between 0°-30°, although, relative to the measured data, it overpredicts the ion current density by nearly 50% at some angles in that range. The measurements show an inflection point near 30°, near the simulated inflection point of 45°; however, the measurements also show a second inflection point near 60°, such that the exponential decay of current density occurs at different rates in these three regions: 5°-30°, 40°-60°, and 60°-150°. Between 150°-180°, the measurements show CEX wings, which agrees with the simulated profile. The measured decay rate in the low-angle region shows good agreement with the simulated decay rate, whereas the decay rates measured in the other two regions are lower than the calculated rates. This results in MPIC1-simulation overpredicting ion current density between 0°-90° and significantly underpredicting between 90°-180°, relative to measured data. For example, relative to the measured data, MPIC1-simulation underpredicts ion current density by as much as 80% at 150°.

MPIC2-simulation calculates larger ion current densities than MPIC1-simulation at low angles, i.e. plume divergence angles of 0°-10°. Between 10°-75°, MPIC2-simulation calculates a lower ion current density than MPIC1-simulation, and between 75°-150°, MPIC2-simulation again calculates a larger ion current density than MPIC1-simulation. MPIC2-simulation calculates an inflection point in ion current density variation at a lower angle than MPIC1: roughly 15°. This is in contrast to the measurements, which show an inflection point near 30°. MPIC2-simulation calculates a second inflection point at roughly 75°, such that ion current density exponentially decays at three different rates in the following ranges: 0°-15°, 20°-75°, and 80°-150°. Between 150°-180°, both the simulated profiles and the measured data show CEX wings. The measured decay rate in the low-angle region shows better agreement with the decay rate calculated by MPIC1-simulation than the rate calculated by MPIC2-simulation, whereas the decay rates measured in the other two regions show better agreement with the rate calculated in MPIC2- rather than MPIC1-simulation. This results in MPIC2-simulation data overpredicting ion current density between 0°-15° and underpredicting between 60°-150°, relative to measured data. However, MPIC2-simulation shows two significant improvements over MPIC1-simulation: first, MPIC2-simulation shows excellent agreement with measured data between 15°-45°; second, although MPIC2-simulation underpredicts measured data at high divergence angles, MPIC2-simulation is in fact in much better agreement with the measurements than MPIC1: for example, relative to the measured data, MPIC1-simulation underpredicts ion current density approximately 81% at 150°, whereas MPIC2-simulation underpredicts measurements by approximately 52%. High plume divergence angle ion current density directly relates to plume impingement concerns stated in Section I. Although, as Figure 27 illustrates, high-angle ion current density is smaller than low-angle current density by nearly 4 orders of magnitude, ions that constitute high-angle ion current density are more likely to impinge on key spacecraft systems. Therefore, accurately resolving high-angle current density is an important metric for assessing each computational model.

The integrated beam currents based on the profiles in Figure 27 are as follows: integrating the MPIC1- and MPIC2-simulation profiles results in a beam current of approximately 17.8 A and 18.1 A, respectively; integrating experimental measurements results in a beam current of 21 A. The uncertainty associated with the integrated beam current ranges between $0-50\%$, which the calculated beam currents are both well within. The discharge current for the nominal operating condition is 20 A, lower than the measured integrated beam current and higher than the simulated integrated current. The difference between the discharge current and the measured integrated beam current could be due to facility back-pressure affecting the diagnostics. However, the difference between the discharge current and the simulated integrated beam current is likely due to the method employed in modeling the cathode: the mass flow at the cathode is assumed to contain only neutrals. Since the integrated beam current based on H2- and H3-simulation is lower than the discharge current, it is likely that the mass flow at the cathode is comprised of neutrals and ions.

V. Discussion

Comparisons between MPIC1- and MPIC2-simulation show moderate to good agreement with measured ion current density data. Near the TE plane, the magnitude of MPIC1-simulation ion current density calculations showed better agreement with measured ion current density magnitudes than MPIC2-simulation. However, MPIC2-simulation showed better agreement with measurements than MPIC1-simulation for the majority of the near-field plume. Further, MPIC2-simulation captured distinct trends in the far-field ion current density data, trends that are not resolved in MPIC1-simulation. Finally, MPIC2-simulation showed better agreement with ion current density measurements at high plume divergence angles, as shown in Figure 27, improving agreement with measured data by as much as 45%. Based on MPIC2-simulation's better agreement with measurements in these cases, the post-collision scattering model which MPIC2 utilizes more accurately characterizes the structure of the plume, especially at high divergence angles.

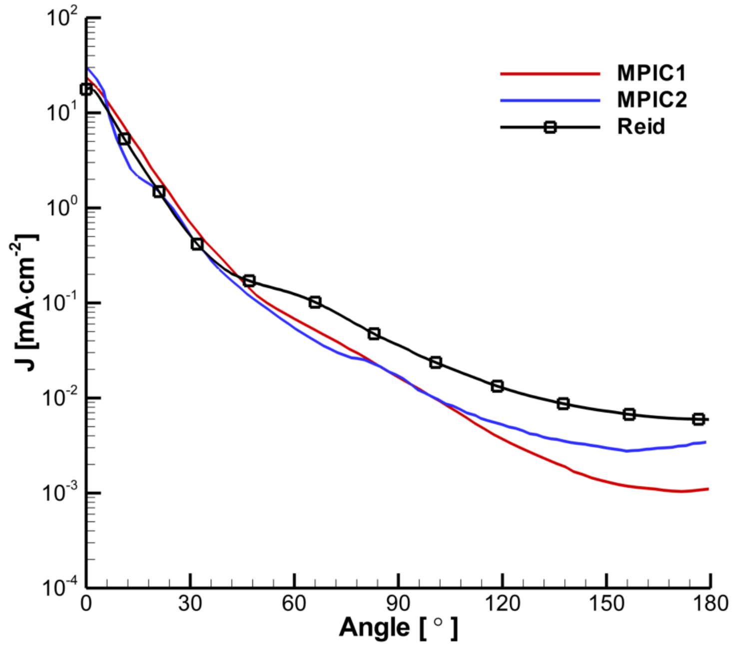

Figure 27. Comparison between MPIC1-simulation, MPIC2-simulation, and experimental measurements: angular variation of far-field ion current density along a 1 m circular arc.

Conclusion

A general purpose hybrid-method code, MPIC, has been supplemented with a new collision dynamics model based on recent experimental measurements. Based on a curve fit to those measurements, the new collision model characterizes post-collision trajectories that were previously unknown. The new collision model improves simulation accuracy in the near- and far-field plume region; e.g., the magnitude of the near-field ion current density "spike" calculated using the new model exhibits a 9.6% improvement in agreement with measured data, whereas high-angle ion current densities calculated using the new model exhibit a 45% improvement in agreement with measured data.

One area of future study to better understand the physical situation in the plume is the characterization of the xenon species at the cathode. Although MPIC2-simulation provides results more accurate than MPIC1-simulation, significant differences still remain between the simulations and measurements regarding the magnitude of the centerline spike in ion current density. As has been previously noted, the mass flow at the cathode is made up of xenon neutrals and ions. The current study assumes a cathode mass flow consisting of only neutrals and this aspect requires further investigation. Another possible area of future investigation is illustrated in the disparity in the magnitude of high divergence angle ion current density between simulated and measured plasma potential data. A possible explanation for this is the fact that the current model does not resolve magnetic field effects, resulting in errors calculating plasma potential gradients in the near-field that subsequently propagate throughout the domain.

Acknowledgments

The authors would like to thank and acknowledge Dr. Justin Koo and Dr. Michelle Scharfe for technical assistance. The authors would also like to thank and acknowledge the Air Force Research Laboratory (AFRL) for funding this work through the Michigan/AFRL Center of Excellence in Electric Propulsion (MACEEP). Dr. Mitat Birkan (AFOSR) and Dr. James Haas (AFRL/RZ) are the joint program managers for this center grant (F9550-09-1-0695).

References

[1]C.R. Koppel and D. Estublier. The smart-1 hall effect thruster around the moon: In flight experience. In *29th International Electric Propulsion Conference*, 2005.

[2]J. Brophy, M.G. Marcucci, G.B. Ganapathi, and C. Gates. Implementation of the dawn ion propulsion system. In *41st AIAA/ASME/SAE/ASEE Joint Propulsion Conference*, 2005.

[3]Y. Choi. *Modeling an Anode Layer Hall Thruster and Its Plume.* Ph.D. Thesis, Dept. of Aerospace Engineering, University of Michigan, Ann Arbor, 2008.

[4]T. Huismann and I.D. Boyd. Modeling of virtual diagnostics for hall thruster plumes in a vacuum-chamber. IEPC Paper 2009-089, Sep 2009.

[5]T. Huismann and I.D. Boyd. Advanced hybrid modeling of hall thruster plumes. In *46th AIAA/ASME/SAE/ASEE Joint Propulsion Conference*, 2010.

[6]G. A. Bird. *Molecular Gas Dynamics and the Direct Simulation of Gas Flows.* Oxford University Press, New York, 1994.

[7]C. K. Birdsall and A. B. Langdon. *Plasma Physics Via Computer Simulation.* Adam Hilger, 1991.

[8]I. D. Boyd and J. T. Yim. Modeling of the near field plume of a hall thruster. *Journal of Applied Physics*, 95(9):4575–4584, 2004.

[9]B. Reid. *The Influence of Neutral Flow Rate in the Operation of Hall Thrusters.* Ph.D. Thesis, Dept. of Aerospace Engineering, University of Michigan, Ann Arbor, 2009.

[10]J. M. Fife. *Hybrid-PIC Modeling and Electrostatic Probe Survey of Hall Thrusters.* Ph.D. Thesis, Department of Aeronautics and Astronautics, Massachusetts Institute of Technology, Cambridge, MA, 1998.

[11]P. Giuliano and I.D. Boyd. Spectral analysis of simulated hall thruster discharge current oscillations. IEPC Paper 2009-084, Sep 2009.

[12]I. D. Boyd. A review of hall thruster plume modeling. Technical Report 2000-0466, January 2000.

[13]J. J. Szabo Jr. *Fully Kinetic Modeling of a Hall Thruster.* Ph.D. Thesis, Department of Aeronautics and Astronautics, Massachusetts Institute of Technology, Cambridge, MA, 2001.

[14]F.I. Parra and et al. A two-dimensional hybrid model of the hall thruster discharge. *Journal of Applied Physics*, 100, 2006.

[15]Shannon Y-M Cheng. *Modeling of Hall thruster lifetime and erosion mechanisms.* Ph.D. Thesis, Department of Aeronautics and Astronautics, Massachusetts Institute of Technology, Cambridge, MA, 2007.

[16]R.R. Hofer, I. Katz, I.G. Mikellides, D.M. Goebel, K.K. Jameson, R.M. Sullivan, and L.K. Johnson. Efficacy of electron mobility models in hybrid-pic hall thruster simulations. In *44th AIAA/ASME/SAE/ASEE Joint Propulsion Conference*, 2008. AIAA-2008-4924.

[17]S. H. Pullins, Y. Chiu, D. J. Levandier, and R. A. Dresseler. Ion dynamics in hall effect and ion thrusters - xe(+) + xe symmetric charge transfer. AIAA Paper 2000-0636, January 2000.

[18]S. Miller, D. J. Levandier, Y. Chiu, and R. A. Dresseler. Xenon charge exchange cross sections for electrostatic thruster models. *Journal of Applied Physics*, 19(3):984–991, 2002.

[19]C. Cai. *Theoretical And Numerical Studies of Plume Flows in Vacuum Chambers.* Ph.D. Thesis, Dept. of Aerospace Engineering, University of Michigan, Ann Arbor, 2005.

[20]I.D. Boyd and M. Crofton. Modeling the plasma plume of a hollow cathode. *Journal of Applied Physics*, 95, 2004.

[21]R. Shastry. *Experimental Characterization of the Near-Wall Region in Hall Thrusters and its Effects on Performance and Lifetime.* Ph.D. Thesis, Dept. of Aerospace Engineering, University of Michigan, Ann Arbor, 2011.